Wetting and spreading of molten volcanic ash in jet engines

*Wenjia Song** [†], *Yan Lavallée* [‡], *Fabian B. Wadsworth*[†], *Kai-Uwe Hess*[†], *and Donald B. Dingwell*[†]

[†] Department of Earth and Environmental Sciences, Ludwig-Maximilians-Universität München, Theresienstrasse 41, 80333 Munich, Germany.

[‡] Earth, Ocean and Ecological Sciences, University of Liverpool, Liverpool, L69 3GP, U.K.

***Corresponding author**: Wenjia Song (wenjia.song@lmu.de)

ABSTRACT

A major hazard to jet engines posed by volcanic ash is linked to the wetting and spreading of molten ash droplets on engine component surfaces. Here, using the sessile drop method, we study the evolution of the wettability and spreading of volcanic ash. We employ rapid temperature changes up to 1040-1450 °C, to replicate the heating conditions experienced by volcanic ash entering an operating jet engine. In this scenario, samples densify as particles coalesce under surface tension until they form a large system-sized droplet (containing remnant gas bubbles and crystals) which subsequently spreads on the surface. The data exhibit a transition from a heterogeneous to a homogeneous wetting regime above 1315 °C as crystals in the drops are dissolved in the melt. We infer that both viscosity and microstructural evolution are key controls on the attainment of equilibrium in the wetting of molten volcanic ash droplets.

TOC GRAPHICS

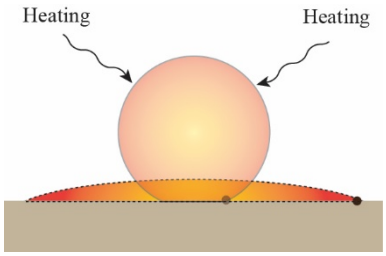

KEYWORDS: Eyjafjallajökull volcano, Wettability, Droplet, Non-isothermal, Rheology.

TEXT

Volcanic ash – comprised of glassy and crystalline fragments smaller than 2 mm - is the most voluminous and widespread product of explosive volcanic eruptions. Such eruptions are increasingly the cause of temporary closure of air travel routes and concomitant economic losses (e.g., the Eyjafjallajökull volcano eruption in Iceland in 2010).[1-7] The "melting" temperature of most volcanic ash is 1000 ~ 1200 °C (depending on the bulk composition);[8] i.e., lower than the turbine inlet temperature (1200 – 1450 °C) of a jet engine at cruising altitude.[9] When ingested, volcanic ash particles are exposed to these high temperatures and melt. The then molten ash impacts and may adhere to hot component surfaces coated by thermal barrier coatings (TBCs) (e.g., nozzle guide vanes and turbine blade surfaces).[10,11] After deposition, the molten volcanic ash may plug the cooling holes and cause the TBC coatings to spall off, potentially exposing the underlying metal surface to highly reactive high temperature gases. Such molten ash deposits can degrade engine performance or even induce catastrophic engine failure.[12-15]

The wetting properties of molten volcanic ash droplets are directly related to processes of impact, adhesion and spreading.[16] Spreading, in particular, controls the contact area and thus the area available for impingement and chemical reaction between ash and the surfaces of high temperature components within a jet engine. Thus, a fundamental understanding of the spreading dynamics of molten volcanic ash droplets is an essential input for generalizing any method of estimation of the propensity for ash deposition as well as any resultant efforts to mitigate the resulting deterioration of jet engine performance.[17]

Previous studies have constrained the spreading of low temperature (<150°C) droplets (e.g., water, organic liquids) whereas others have investigated the behavior of molten metals and glasses at high temperature (1100-1350°C).[18,19] Most analyses of liquid-solid wetting have been

conducted under thermodynamic equilibrium conditions, where all material properties (e.g., viscosity, surface tension, and distribution of phases) are time invariant. In contrast, under non-isothermal conditions, as is the case during ingestion and deposition of ash in operating jet engines, the material properties vary through time. Such complex thermal scenarios require investigation of the spreading kinetics under dynamic conditions. Until such dynamic scenarios are experimentally investigated, our understanding of the wetting properties of volcanic ash on jet engine surfaces must remain rudimentary.

Here, we present experimental results of wetting under highly dynamic conditions by directly exposing volcanic ash to high temperatures (between 1039°C and 1451°C), designed to replicate the heating conditions experienced by the volcanic ash entering an operating jet engine. These results should enable a scaling analysis of the most complex and relevant dynamic case of ash – turbine interaction 1) where spreading occurs mainly under non-isothermal conditions, 2) for which the suspended crystalline phase fraction in the viscous droplets decreases as a function of time as crystals melt/dissolve, and 3) where wholesale spreading is preceded by a coalescence process of many smaller droplets - analogous to multiple impacts of volcanic ash particles on surfaces.

The present sessile drop experiments were performed using volcanic ash-sized particles, produced by crushing a much larger volcanic bomb sample from the 2010 eruption of Eyjafjallajökull volcano, Iceland. The bulk chemical composition, microstructure, and particle size distribution of the lab-produced ash were obtained using X-ray fluorescence, scanning electron microscopy (SEM), and laser diffraction methods, respectively (for details see Text S1 and Figure S1 in the supporting information).

Volcanic ash samples (with grain sizes of < 63 μm) were first compressed under an applied stress (1.5 N mm^{-2}) into 3-mm high, 3-mm diameter cylinders which were then placed on an alumina (99.99%) substrate (10 × 12 mm). This sample assembly (i.e. ash cylinder plus alumina substrate) was then fixed in the sample holder of an optical dilatometer (Figure 1A).[20] To test the effect of rapid heating conditions (and thereby to simulate in a controlled manner the non-isothermal conditions approaching those experienced by volcanic ash upon ingestion into a jet engine), we have adopted a procedure in which the sample assembly (at position a; Figure 1A) was inserted into the furnace (at position b; Figure 1A), which had been preheated to a target temperature $\boldsymbol{T_{max}}$. The temperature of the furnace $\boldsymbol{T_{max}}$ was set in successive experiments to temperatures ranging between 1039 ºC and 1451 ºC. After the compacted sample was inserted in the furnace hot zone, morphological changes of the compact were monitored at a 1 Hz sampling rate by a charge-coupled device (CCD) camera, which captured 2D cross-sectional images of the cylinder parallel to the axis of rotation.

In this optical dilatometer, a thermocouple and its alumina sheath are inserted into an alumina protective tube to protect the thermocouple against chemical contamination. In order to minimize the heat-retarding effect of the thermal mass of the sheath and to better constrain actual temperature path experienced by the sample, we have conducted a separate set of calibration experiments wherein a second (unsheathed) S-type thermocouple (Figure 1B), was located on the alumina substrate in the same position as the compacted volcanic ash sample (Text S2 and Figures S2 and S3). The sample was kept at high temperature until the spreading reached equilibrium conditions, defined as the optical observation of the cessation of spreading.[21] The experiments at each temperature were repeated at least three times. These wetting processes are visually illustrated in the Movie S1.

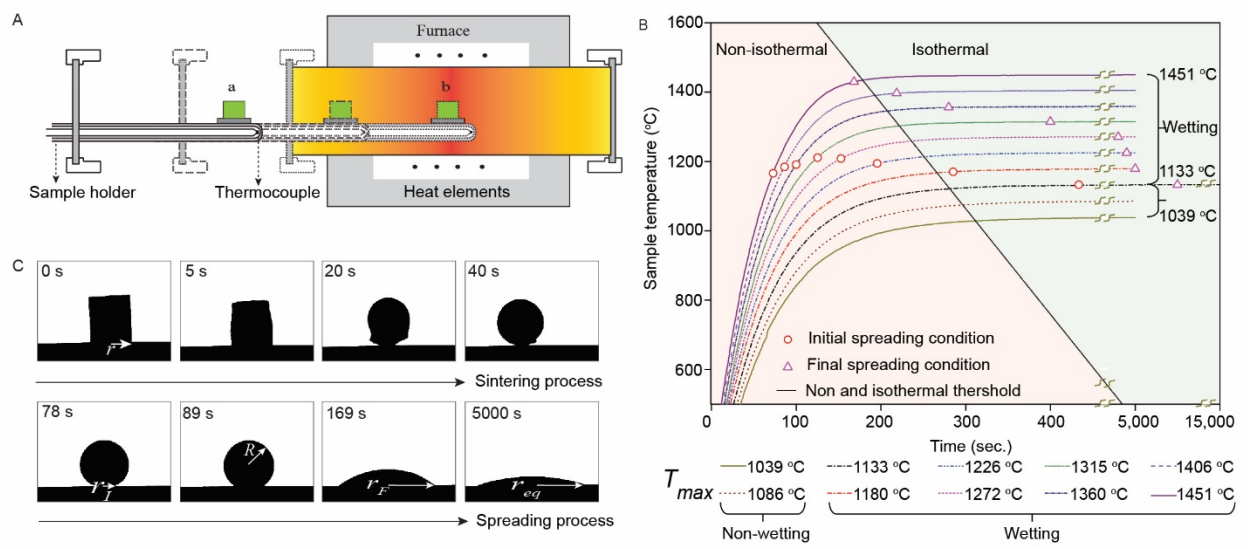

Figure 1. Thermal history in the wetting experiments at the various heating conditions. (A) Side view of the setup and sessile drop method during rapid heating: the volcanic ash compact, which is placed outside the furnace (Position a), was rapidly moved into the hot zone (Position b) after the furnace was heated up to the desired temperature; subsequently, geometric parameters were tracked with time. (B) Sample temperature-time profiles measured by the thermocouple without alumina tube protection at the $\boldsymbol{T_{max}}$ from 1039 °C to 1451 °C at intervals of 47 °C. (C) Sintering and subsequent spreading of molten volcanic ash droplets for experiments with $\boldsymbol{T_{max}}$ of 1451 °C, represented by a series of photographs showing the melting of a 3×3 mm volcanic ash compact. Note that the field of view is 10-mm wide × 6-mm high.

Once inserted at $\boldsymbol{T_{max}}$, the samples decreased non-linearly in cross-sectional area $\boldsymbol{A}$ axisymmetrically, and therefore in volume,[22] we observe that for $\boldsymbol{T_{max}}$ < 1133 °C, spreading of the contact line does not occur on the timescales of our experiments, whereas above this value, spreading is observed to be time-dependent. This critical temperature is in good agreement with the sample liquidus 1141 °C, above which the system is likely fully molten (as constrained by using major element chemistry shown in Figure S1A, but excluding water content, as input into the MELTS thermodynamic multicomponent calculator).[23,24] This implies that for multiphase volcanic droplets suspending crystals, the liquidus temperature may be a first-order constraint on

the likelihood of jet engine component surface suffering the impact of wetting during the ingestion of volcanic ash particles.

Combined analysis of the heating profile and spreading conditions (Figure 1B) indicates that in experiments conducted at low temperature regime at 1133 °C ≤ $\boldsymbol{T_{max}}$ ≤ 1180 °C, the entire spreading process occurs under effectively isothermal conditions. In the higher temperature regime however, namely, at 1226 °C ≤ $\boldsymbol{T_{max}}$ ≤ 1451 °C, the spreading process initiates and develops mainly under non-isothermal conditions. Thus in the scenarios studied here (as well as any, more extreme, heating conditions) the spreading of molten volcanic ash droplets is not a purely isothermal process occurring at a constant state, but rather a complex physico-chemical process (involving the glass transition, crystal melting and likely volatile exsolution and outgassing). Moreover, under such rapid heating conditions, melting itself is a substantially disequilibrium process as melting may result from the dissolution of individual minerals, leading to complex microstructure evolution as minerals melt, and the resultant melts mingle and mix (i.e., chemically homogenize), perhaps causing a transient rheological response upon spreading.[25,26]

In these tests, performed to simulate ash ingestion in hot engines, spreading does not commence instantaneously,[27] but rather initially requires sintering of the constituent particles, whereby the sample may shrink due to particles coalescing. Once the interstitial gas phase has become isolated from the outside of the sample (complete sintering), the sample can swell in size if the temperature continues to increase due to gas expansion in the now-trapped pores (see upper row in Figure 1C, at the $\boldsymbol{T_{max}}$ of 1451°C and Text S3 and Figure S4).[28] During sintering, the original cylindrical compact of volcanic ash melts to form a volcanic ash droplet with a volume of ca. 3 mm^{-3}, which is then amenable to spreading (during spreading, the sample-substrate

contact surface widens radially, defined by a circular area of radius $\boldsymbol{r}$; see lower row in Figure 1C). From this point forward, in order to quantify the onset and end of spreading, we use the evolution of the radius $\boldsymbol{r(t)}$ (between the molten volcanic ash and solid alumina substrate) to define the initial, final and equilibrium spreading conditions: these radius and time conditions are expressed as $\boldsymbol{r_I}$, $\boldsymbol{r_F}$, $\boldsymbol{r_{eq}}$ and $\boldsymbol{t_I}$, $\boldsymbol{t_F}$, $\boldsymbol{t_{eq}}$ respectively (see lower row in Figure 1C) (Text S4 and Figure S5). A maximum value of shape factor $\boldsymbol{S}$ (defined by $\boldsymbol{S = 4\pi A/P^2}$ where $\boldsymbol{A}$ and $\boldsymbol{P}$ are the 2D sample cross section area and perimeter) after the initial spreading condition is used to characterize the droplet radius itself as a droplet of initial radius $\boldsymbol{R}$ (e.g., at 89 s of a wetting experiment at $\boldsymbol{T_{max}}$ of 1451 °C). Details and worked examples are given in Table S1.

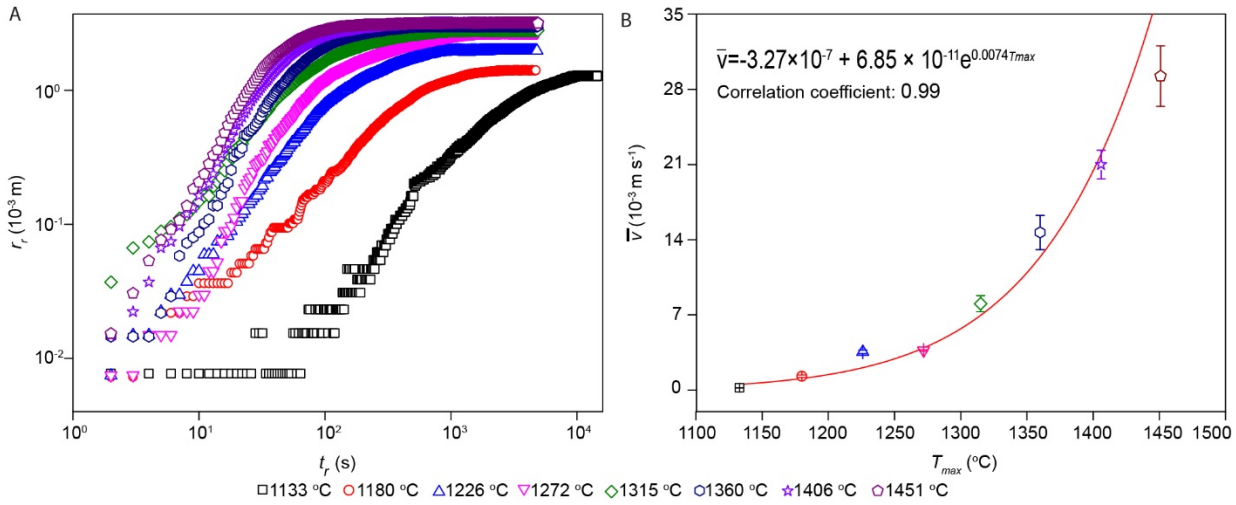

Figure 2. The spreading dynamics of the molten volcanic ash droplets at the various heating conditions. (A) Evolution of the relative spreading radius $\boldsymbol{r_r}$ plotted as a function of relative time $\boldsymbol{t_r}$ for the molten volcanic ash droplets from the initial stage of spreading until equilibrium at $\boldsymbol{T_{max}}$ from 1133 °C to 1451 °C. (B) Mean spreading velocity $\boldsymbol{\bar{v}}$ of the molten volcanic ash droplets in the range between the initial and finial spreading conditions as a function of $\boldsymbol{T_{max}}$. The data in Figure 2A represent individual experimental datasets while the data in Figure 2B show the mean of three independent experiments, along with the standard deviation. We give a functional approximation (red curve) of the temperature dependence of the mean spreading rate for these droplet sizes.

Our experimental results yield first and foremost insights into the dynamics of the spreading process when $\boldsymbol{T_{max}}$ is 1133-1451°C, namely, how the wetted area of radius $\boldsymbol{r}$ grows with the time $\boldsymbol{t}$ once a molten volcanic ash drop spreads shown in the second row of Figure 1C at the variety of $\boldsymbol{T_{max}}$. To easily compare the process at each temperature, we adopt the relative spreading radius $\boldsymbol{r_r}$, defined as $\boldsymbol{r - r_I}$, plotted as a function of the relative time $\boldsymbol{t_r}$, defined as $\boldsymbol{t - t_I}$, at $\boldsymbol{T_{max}}$ of between 1133°C to 1451°C are shown in Figure 2A. We observe that during the initial spreading process at low $\boldsymbol{T_{max}}$ between 1133°C and 1180°C, $\boldsymbol{r_r}$ increases as a function of time, which indicates even spreading occurs during essentially isothermal condition. The dominant material property which varies by orders of magnitude over relatively small changes in temperature, is the silicate liquid viscosity $\boldsymbol{\mu}$. Therefore, it is important to constrain the temperature dependence of the viscosity (see below).

To provide an empirical tool of wider utility for the average kinetics of spreading, we assess the average spreading velocity $\overline{\boldsymbol{v}}$ (denoting the mean of the velocity $\boldsymbol{dr_r/dt_r}$ between the initial and final spreading conditions) (Text S5). We note that $\overline{\boldsymbol{v}}$ increases approximately exponentially with the ambient temperature above the glass transition (the best-fit exponential function is given in Figure 2B), further confirming that temperature is a key parameter in controlling the spreading rate and wetting propensity of molten volcanic ash droplets.

Upon completion of the spreading of molten volcanic ash droplets (namely, after 1.5 $\times 10^4$ s at the $\boldsymbol{T_{max}}$ = 1133 °C and 5 ×103 s for $\boldsymbol{T_{max}}$ > 1133 °C), we measure the average equilibrium contact angle $\boldsymbol{\theta_{eq}}$ as the mean of the contact angle on the right and left side of the sample (Figure 3A). We show that $\boldsymbol{\theta_{eq}}$ is a strong function of $\boldsymbol{T_{max}}$ and apparently approaches a temperature-independent low-angle value at high $\boldsymbol{T_{max}}$ (Figure 3A). Furthermore, we use the model based on

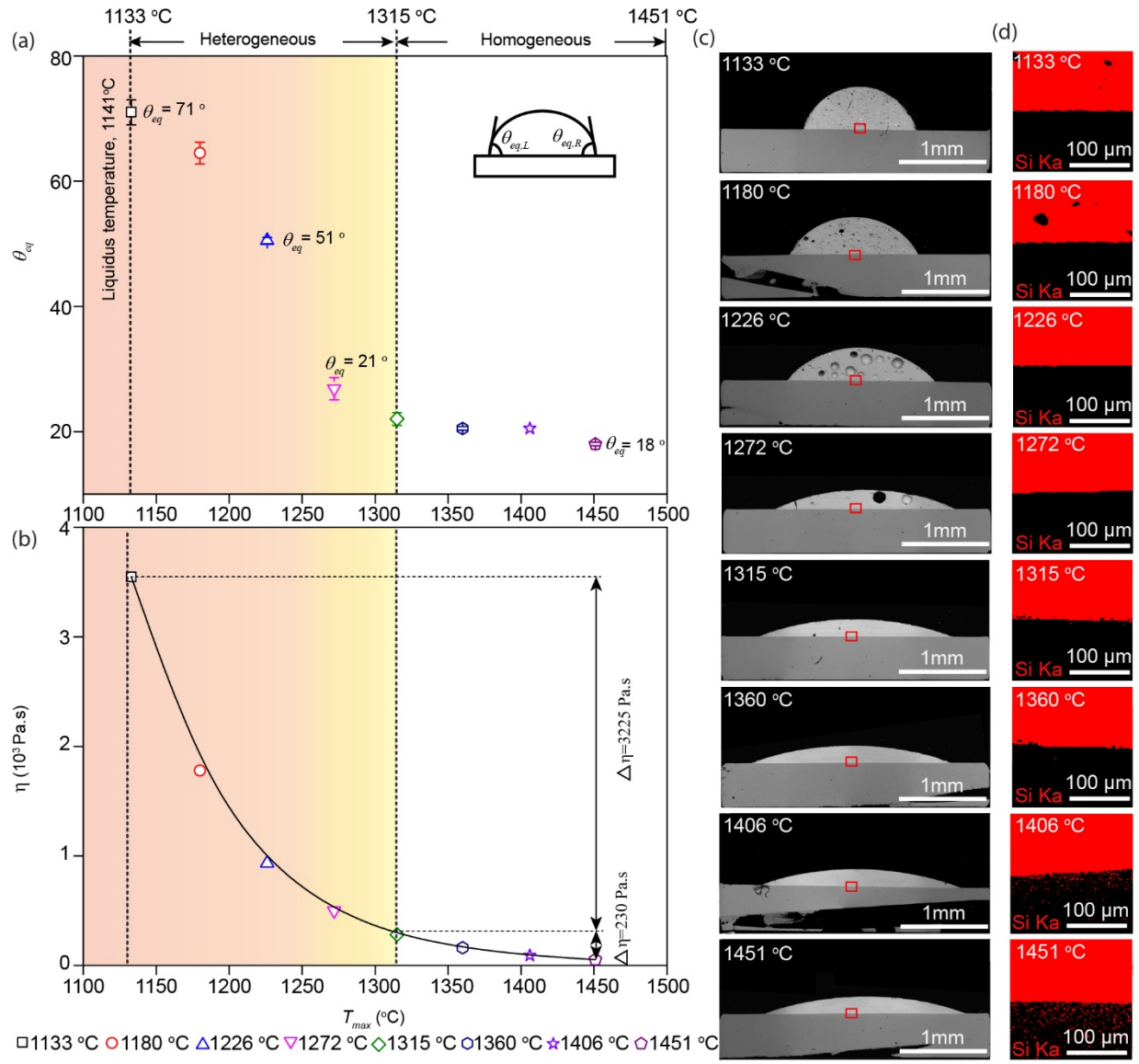

Figure 3. Equilibrium wetting state of molten volcanic ash droplets at various heating conditions. (A) Dependence of the equilibrium contact angle θ_{eq} of molten volcanic ash droplets on $\boldsymbol{T_{max}}$. Inset: a schematic illustration of the left and right side of the sample, yielding two measurements per sample. (B) Viscosity of molten volcanic ash based on concentric cylinder measurements (see Supplementary Information). (C) SEM photographs of the interior microstructural evolution of the spreading volcanic ash with an increasing$\boldsymbol{T_{max}}$. (D) Si element maps showing the extent of molten volcanic ash droplets penetration at various $\boldsymbol{T_{max}}$. The images in Figures 3C and 3D show representative textures obtained at each testing condition.

the experimentally determined viscosity values, Text S6 and Figure S6 obtained from the volcanic ash melt without crystals and bubbles and under thermodynamic equilibrium conditions to calculate the viscosity value at each $\boldsymbol{T_{max}}$ shown in Figure 3B. Considering the existence of bubbles and crystals at low $\boldsymbol{T_{max}}$ (1133 °C ≤ 1272 °C; Figure 3C), the actual bulk viscosity values are possibly higher than the calculated ones. Surface tension is apparently negligibly dependent on temperature.[29] However, even small changes in surface tension can manifest as large differences in contact angle.[30] The effect of viscosity strongly controls the kinetics of the approach to equilibrium contact angle (see below). Analysis of the cross-sectional area of the droplet after the experiment shows the evolution of internal microstructure with an increasing T_{max} (Fig. 3c). The threshold T_{max} 1315°C could be regarded as a transition in microstructure evolution defining heterogeneous and homogenous regimes.

Chemical analysis across the sample-substrate interface indicates that Si undergoes no obvious sign of interdiffusion at $\boldsymbol{T_{max}}$ ≤ 1315°C (Figure 3D). In contrast, at $\boldsymbol{T_{max}}$ > 1315°C, there is evidence of chemical exchange between the sample and the substrate. However, even at the $\boldsymbol{T_{max}}$ = 1451°C, the penetration depth is 150 μm (i.e., far less than the 1-mm thick alumina substrate) and the relative difference of viscosity caused by interdiffusion is lower than 7 %, (using a multicomponent viscosity model calibrated for silicate melts (Text S7 and Figure S7)).[31,32] This constraint suggests that it may be reasonable to regard the spreading process (under the temperature conditions and timescales explored in this study) as occurring under relatively inert (non-reactive) conditions.

Generally, the dynamics of droplets impacting, depositing and spreading on surfaces are characterized by the Eötvös, Ohnesorge, and Weber numbers.[33] The Eötvös number $\mathbf{Eo} = \boldsymbol{\rho g R^2}/\Gamma$ scales the relative importance of gravitational and surface tension forces, where $\boldsymbol{\rho}$ is the

liquid density, Γ is the surface tension and $\boldsymbol{R}$ is the characteristic droplet size. The Ohnesorge number $\mathbf{Oh} = \boldsymbol{\mu}/\sqrt{\boldsymbol{\rho}\Gamma\mathbf{R}}$ scales the relative importance of viscous forces and inertia arising from surface tension forces. The Weber number $\boldsymbol{We} = \boldsymbol{\rho R u^2}/\Gamma$ scales the relative importance of inertia and surface tension forces, where $\boldsymbol{u}$ is the impact velocity of the droplet. For volcanic ash droplets, across a wide range of temperatures between 1100-1600 °C, $\boldsymbol{\rho}$ is 2000-2895 kg m^{-3}, $\boldsymbol{R}$ is 10^{-7}-10^{-2} m (and milled to <10^{-5} m in jet engine compressor[16]), and Γ is 0.35-0.37 N m^{-1} (for this scaling analysis, we choose the average value 0.36 as a mean value);[34-36] and therefore, $\mathbf{Eo}$ < 1 whereby surface tension dominates over body forces. As a large number of volcanic droplets are deposited on a surface they coalesce under surface tension forces at droplet-droplet interfaces, and can form much larger droplets. However for $\mathbf{Eo}$ to exceed unity, the droplets would have to reach ~10^{-2} m, which is unlikely in jet engines. Therefore, the effect of gravity on the droplet scale can be neglected. Previous studies have focused on the low $\mathbf{Eo}$ number regime in which small droplets spread on surfaces (as here) and where the role of gravity is negligible. In this case the main body of work has focused on either (1) the high $\mathbf{Oh}$ number case where spreading is driven by capillarity at the contact line or (2) low $\mathbf{Oh}$ number droplets for which the Weber number is high, which is not the case here (in our case $\boldsymbol{u} = \mathbf{0}$ and so $\mathbf{We} \rightarrow \mathbf{0}$).[37]

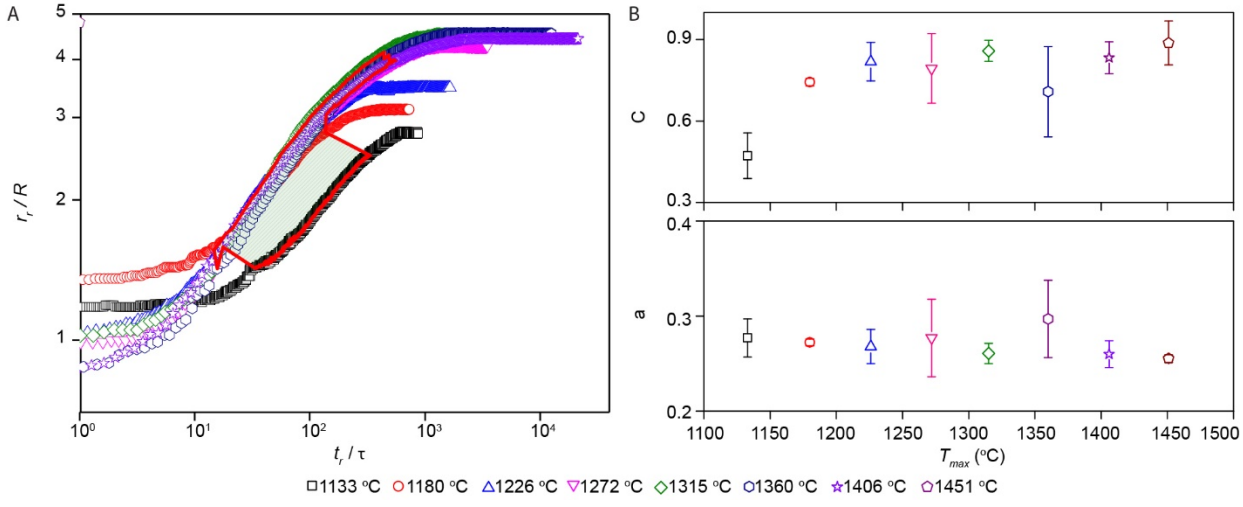

Figure 4. Scaling the wetting process using volcanic ash. (A) Dimensionless radius $\boldsymbol{r_r/R}$ as a function of the dimensionless time $\boldsymbol{t_r/\tau}$, with $\boldsymbol{\tau = R\mu/\Gamma}$ for the data from Figure 2A. (B) Dynamic coefficients *C* and α as a function of $\boldsymbol{T_{max}}$. The data in Figure 4a represent individual experimental dataset and the data in Figure 4B show the mean of three independent experiments, along with the standard deviation.

Where a wetting liquid droplet contacts a solid surface in the high $\mathbf{Oh}$, low $\mathbf{We}$ number regimes, the kinetics of droplet spreading can be scaled by Tanner's law which is cast as $\boldsymbol{r/R = (t/\tau)^{1/10}}$,[38,39] where $\boldsymbol{\tau}$ is the capillary timescale $\boldsymbol{\tau = R\mu/\Gamma}$ (Text S8).[40] This scaling has not however proved universal when tested against experimental data and thus a more general empirical scaling has been proposed $\boldsymbol{r/R = C(t/\tau)^{a}}$ where $\boldsymbol{a}$ is proportional to the contact angle between the droplet and substrate.[41] Variations of these propositions have been tested over a large range of experimental complexity. In non-isothermal conditions, as is the case during ingestion and deposition of ash in operating jet engines, the material properties vary with time upon heating. Non-isothermal conditions can be incorporated in the scaling for $\boldsymbol{r/R}$ by rendering $\boldsymbol{\tau}$ a function of time.

To illustrate a scaling of the adapted form of Tanner's Law presented above, in Figure 4A we normalize $\boldsymbol{r_r}$ by $\boldsymbol{R}$ and $\boldsymbol{t_r}$ by $\boldsymbol{\tau}$. Here, we use $\boldsymbol{\mu(T,t)}$ (see Figure 3B) to compute $\boldsymbol{\tau}$ at each temperature during thermal equilibration to $\boldsymbol{T_{max}}$ based on experimental viscosity measurement. Most datasets collapse to a single curve via this normalization. The exception is for the experiments conducted at 1133°C and at 1180°C, presumably because at these temperatures the sample was not completely molten and therefore, $\boldsymbol{\mu(T,t)}$ does not capture the viscosity of the bulk material. This convergence confirms that capillarity is driving spreading and thus viscosity is rate-limiting.

Tanner's law is generally applied for predicting the late-stage spreading of droplets instead of the initial development of spreading. Therefore, in order to obtain the cut-off point between the early- and late-stage regime of spreading process at each temperature condition, we apply the Pearson product-moment correlation coefficient ζ to verify the power law relationship of a modified Tanner's law (for the details on Pearson product-moment correlation coefficient, see Text S9, Figure S8) and classify the spreading process into two stages: the early and late spreading stage.[42] The onset of the late spreading stage is marked with a red line (Figure 4A), which represents a perfect power-law with a correlation coefficient greater than 0.99. We apply the empirical modification of Tanner's law described above and observe that in our experiment, the values of C and a (for molten volcanic ash droplets spreading under the different temperatures by fitting the data marked in red in Figure 4A) are almost universal (0.76 ± 0.13 and 0.27 ± 0.01, respectively), unlike the spreading characteristics of an ideal drop (e.g., water and metal) at low or high temperatures as both of these parameters would vary with the droplet properties.[43,44]

This study quantifies how rapidly volcanic ash may be expected to melt, coalesce and spread during rapid heating to high temperatures, similar to those encountered within operating jet engines. The analysis of post-coalescence spreading dynamics of molten volcanic ash droplet under the different $\boldsymbol{T_{max}}$ conditions establishes that the liquidus temperature is the threshold to wetting and spreading of volcanic ash, that capillarity controls spreading kinetics and that the temperature-dependent viscosity is the dominant rate-limiting parameter, indicating that temperature is the most important parameter controlling the deposition propensity in jet engines. The data suggest that under such rapid heating conditions, which impose non-isothermal conditions, the spreading kinetics can be scaled by adopting a non-isothermal capillary timescale.

Our experiments reveal fundamental similarities in the spreading behavior of molten volcanic ash and pure liquid at high temperatures despite their additional complexities. These results can serve as a basis for the formulation of a unified wetting and spreading theory in high temperature systems of industrial interest and may motivate the development of specific non-wetting barrier coatings for jet engine parts.

ASSOCIATED CONTENT

Supporting Information provides additional technical details on the Eyjafjallajökull volcanic ash characterization, measurement of the sample temperature, definition of characteristic conditions in spreading process, definition of average spreading velocity, viscosity measurement of volcanic ash melt, the sensitization of molten volcanic ash on interfacial effects, rescaling the spreading process based on Tanner'law, Pearson product-moment correlation coefficient analysis as well as movie for showing the wettability and spreading process of volcanic ash at the extreme heating conditions.

ACKNOWLEDGMENT

We are grateful to Corrado Cimarelli for providing the sample material, to Stephan Kolzenburg for viscosity measurement, Michaela Ridder for SEM measurements and to Paul Ayris, Ulrich Kueppers, Zsuzsanna Major from Max Plank Institute of Quantum Optics and Axel Hesse from Hesse Instruments for fruitful discussions and Andre Schöttler-Himmel for IT support. Wenjia Song acknowledges the Alexander von Humboldt Foundation for a postdoctoral fellowship held at the onset of this project and the support of LMU Munich‘s Institutional Strategy LMUexcellent within the framework of the German Excellence Initiative during the revision of this manuscript. We also acknowledge the support from the ‘Freigeist’ Fellowship of the VolkswagenStiftung to Wenjia Song on “Volcanic Ash Deposition in Jet Engines” (VADJEs,

No 89705), and the European Research Council for the ERC Advanced Grant to Dingwell on "Explosive Volcanism in the Earth System" (EVOKES, No 247076) as well as the ERC Starting Grant to Lavallée on "Strain Localisation in Magmas" (SLiM, No 306488).

REFERENCES

(1) Webley, P.; Mastin, L. Improved prediction and tracking of volcanic ash clouds. *J. Volcanol. Geotherm. Res.* **2009**, 186, 1-9, DOI: 10.1016/j.jvolgeores.2008.10.022.

(2) Sanderson, K., Questions fly over ash-cloud models. *Nature* **2010**, 464, 1253, DOI: 10.1038/4641253a.

(3) Sigmundsson, F.; Hreinsdóttir, S.; Hooper, a.; Árnadóttir, T.; Pedersen, R.; Roberts, M. J.; Óskarsson, N.; Einarsson, A. L.; Geirsson, H.; Hensch, M.; Ófeigsson, B. G.; Sturkell, E.; Sveinbjörnsson, H.; Feigl, K. L. Instrusion triggering of the 2010 Eyjafjallajökull explosive eruption. *Nature* **2010**, 468, 426-430, DOI: 10.1038/nature09558.

(4) Dingwell, D. B.; Lavallée, Y.; Kueppers, U. Volcanic ash: a primary agent in the earth system. *Phys. Chem. Earth Pt. A* **2012**, 45-46, 2-4, DOI: 10.1016/j.pce.2011.07.007.

(5) Gudmundsson, M. T.; Thordarson, T.; Höskuldsson, Á.; Larsen, G.; Björnsson, H.; Prata, F. J.; Oddsson, B.; Magnússon, E.; Högnadóttir, T.; Petersen, G. N.; Hayward, C. L.; Stevenson. J. A.; Jónsdóttir, I. Ash generation and distribution from the April-May 2010 eruption of Eyjafjallajökull, Iceland. *Sci. Rep.* **2012**, 2, 1-12, DOI: 10.1038/srep00572.

(6) Houghton, I. M. P.; Aplin, K. L.; Nicoll, K. A. Triboelectric charging of volcanic ash from the 2011 Grímsvötn eruption. *Phys. Rev. Lett.* **2013**, 111, 118501, DOI: 10.1103/PhysRevLett.111.118501.

(7) Kueppers, U.; Cimarelli, C.; Hess, K. U.; Taddeucci, J.; Wadsworth, F. B.; Dingwell, D. B. The thermal stability of Eyjafjallajökull ash versus turbine ingestion test sands. *J. Appl. Volcanol.* **2014**, 3, 4, DOI: 10.1186/2191-5040-3-4.

(8) Song, W.; Lavallée, Y.; Hess, K. U.; Kueppers, U.; Cimarelli, C.; Dingwell D. B. Volcanic ash melting under conditions relevant to ash turbine interactions. *Nat. Commun.* **2016**, 7, 10795, DOI: 10.1038/ncomms10795.

(9) Laycock, R. G.; Fletcher T. H. Time-dependent deposition characteristics of fine coal fly ash in a laboratory gas turbine environment. *J. Turbomach.* **2013**, 135, 021003, DOI: 10.1115/1.4006639.

(10) Padture, N. P.; Gell, M.; Jordan E. H. Thermal barrier coatings for gas-turbine engine applications. *Science* **2002**, 296, 280-284, DOI: 10.1126/science.1068609.

(11) Taltavull, C.; Dean, J.; Clyne, T. W. Adhesion of volcanic ash particles under controlled conditions and implications for their deposition in gas turbines. *Adv. Eng. Mater.* **2015**, 18, 803-813, DOI: 10.1002/adem.201500371.

(12) Dunn, M. G.; Padova, C.; Moller, J. E.; Adams, R. M. Performance deterioration of a turbofan and a turbojet engine upon exposure to a dust Environment. *J. Eng. Gas Turbines Power* **1978**, 109, 336-343, DOI: 10.1115/1.3240045.

(13) Kim, J.; Dunn, M. G.; Baran, A. J.; Wade, D. P.; Tremba, E. L. Deposition of volcanic materials in the hot sections of two gas turbine engines. *J. Eng. Gas Turbines Power* **1993**, 115, 641-651, DOI: 10.1115/1.2906754.

(14) Drexler, J. M.; Gledhill, A. D.; Shinoda, K.; Vasiliev, A. L.; Reddy, K. M.; Sampath, S.; Padture, N. P. Jet engine coatings for resisting volcanic ash damage. *Adv. Mater.* **2011**, 23, 2419-2424, DOI: 10.1002/adma.201004783.

(15) Dunn, M. G. Operation of gas turbine engines in an environment contaminated with volcanic ash. *J. Turbomach.* **2012**, 134, 051001, DOI: 10.1115/1.4006236.

(16) Dean, J.; Taltavull, T. W.; Clyne, T. W. Influence of the composition and viscosity of volcanic ashes on their adhesion within gas turbine aeroengines. *Acta Mater*. **2016**, 109, 8-16, DOI: 10.1016/j.actamat.2016.02.011.

(17) Perepezko, J. H. The hotter the engine, the better. *Science* **2009**, 326, 1068-1069, DOI: 10.1126/science.1179327.

(18) Saiz, E.; Tomsia A. P. Atomic dynamics and Marangoni films during liquid-metal spreading. *Nat. Mater*. **2004**, 3, 903-909, DOI: 10.1038/nmat1252.

(19) Schmitz. J.; Brillo, J.; Egry, I. Surface tension of liquid Cu and anisotropy of its wetting of sapphire. *J. Mater. Sci*. **2010**, 45, 2144-*2149*, DOI: 10.1007/s10853-010-4212-2.

(20) Song, W.; Hess, K. U.; Damby, D. E.; Wadsworth, F. B.; Lavallée, Y.; Cimarelli, C.; Dingwell, D. B. Fusion characteristics of volcanic ash relevant to aviation hazards. *Geophys. Res. Lett*. **2014**, 41, 2326-2333, DOI: 10.1002/2013GL059182

(21) Bonn, D.; Eggers, J.; Indekeu, J.; Meunier, J.; Rolley, E. Wetting and spreading. *Rev. Mod. Phys*. **2009**, 81, 739-805, DOI: 10.1103/RevModPhys.81.739.

(22) Wadsworth, F. B.; Vasseur, J.; von Aulock F. W.; Hess, K.-U.; Scheu, B.; Lavallée, Y.; Dingwell, D. B. Nonisothermal viscous sintering of volcanic ash. *J. Geophys. Res. Solid Earth* **2014**, 119, 8792-8804, DOI: 10.1002/2014JB011453.

(23) Ghiorso, M. S.; Sack, R. O. Chemical mass transfer in magmatic processes IV. A revised and internally consistent thermodynamic model for the interpolation and extrapolation of liquid-solid equilibria in magmatic systems at elevated temperatures and pressures. *Contrib. Mineral. Petrol*. **1995**, 119, 197-212, DOI: 10.1007/BF00307281.

(24) Asimow, P. D.; Ghiorso, M. S. Algorithmic modifications extending MELTS to calculate subsolidus phase relations. *Am. Mineral.* **1998**, 83, 1127-1132, DOI: http://www.asimow.com/reprints/AmMin_83_1127.pdf.

(25) Kendrick, J. E.; Lavallée, Y.; Hirose, T.; Di Toro, G.; Hornby, A. J.; De Angelis, S.; Dingwell, D. B. Volcanic drumbeat seismicity caused by stick-slip motion and magmatic frictional melting, *Nat. Geosci.* **2014**, 7, 438-442, DOI: 10.1038/ngeo2146.

(26) Hornby, A. J.; Kendrick, J. E.; Lamb, O. D.; Hirose, T.; De Angelis, S. F.; von Aulock. W.; Umakoshi, K.; Miwa, T.; De Angelis, H. S.; Wadsworth, F. B.; Hess, K. U.; Dingwell, D. B.; Lavallée, Y. Spine growth and seismogenic faulting at Mt. Unzen, Japan. *J. Geophys. Res. Solid Earth* **2015**, 120, 4034-4054, DOI: 10.1002/2014JB011660.

(27) Eddi, A.; Winkels, K. G.; Snoeijer, J. H. Short time dynamics of viscous drop spreading. *Phys. Fluids* **2013**, 25, 013102, DOI: 10.1063/1.4788693.

(28) Wadsworth, F. B.; Vasseur, J.; Llewllin, E. W.; Schauroth, J.; Dobson, K. J.; Scheu, B.; Dingwell, D. B. Sintering of viscous droplets under surface tension. *Proc. R. Soc. A* **2016**, 472, 20150780, DOI: 10.1098/rspa.2015.0780.

(29) Gardner, J. E.; Ketcham, R. A.; Moore, G. Surface tension of hydrous silicate melts: Constraints on the impact of melt composition. *J. Volcanol. Geoth. Res.* **2013**, 267, 68-74, DOI: http://dx.DOI.org/10.1016/j.jvolgeores.2013.09.007.

(30) Schiaffino, S.; Sonin, A. A. Molten droplet deposition and solidification at low Weber numbers. Phys. Fluids **1997**, 9, 3172-3187, DOI: http://dx.DOI.org/10.1063/1.869434.

(31) Giordano, D.; Russell, J. K.; Dingwell, D. B. Viscosity of magmatic liquids: a model. *Earth Planet. Sci. Lett.* **2008**, 271, 123-134, DOI:10.1016/j.epsl.2008.03.038.

(32) Landry, K.; Eustathopoulos, N. Dynamics of wetting in reactive metal/ceramic systems: linear spreading. *Acta. Mater.* **1996**, 44, 3923-3932, DOI: 10.1016/S1359-6454(96)00052-3.

(33) Han, J.; Tryggvason, G. Secondary Breakup of Liquid Drops in Axisymmetric Geometry—Part I, Constant Acceleration. *Phys. Fluids* **1999**, 11, 3650-3667, DOI: 10.1063/1.870229.

(34) Lange, R. A. A revised model for the density and thermal expansivity of K_2O-Na_2O-CaO-MgO-Al_2O_3-SiO_2 liquids from 700 to 1900 K: extension to crustal magmatic temperatures. *Contrib. Mineral. Petrol.* **1997**, 130, 1-11, DOI: 10.1007/s004100050345.

(35) Heiken, G. *An atlas of volcanic ash*; Smithsonian Inst. Press: Washington, USA, 1974.

(36) Walker, D.; O. Mullins. Surface tension of natural silicate melts from 1,200°–1,500°C and implications for melt structure. *Contrib. Mineral. Petrol.* **1981**, 76, 455-462, DOI: 10.1007/BF00371487.

(37) Leger, L.; Joanny, J. F. Liquid spreading. *Rep. Prog. Phys.* **1997**, 55, 431-486, DOI: 0034-4885/55/4/001.

(38) Tanner, L. H. The spreading of silicone oil drops on horizontal surfaces. *J. Phys. D: Appl. Phys.* **1979**, 12, 1473-1484, DOI: 10.1088/0022-3727/12/9/009**.**

(39) Rafaï, S.; Sarker, D.; Bergeron, V.; Meuier, J.; Bonn, D. Superspreading: aqueous surfactant drops spreading on hydrophobic surfaces. *Langmuir* **2002**, 18, 10486-10488, DOI: 10.1021/la020271i.

(40) Wang, J.; Do-Quang, M.; Cannon, J. J.; Yue, F.; Suzuki, Y.; Amberg, G.; Shiomi, J. Surface structure determines dynamic wetting. *Sci. Rep.* **2015**, 5, 8474, DOI: 10.1038/srep08474.

(41) Courbin, L.; Bird, J. C.; Reyssat, M.; Stone, H. A. Dynamics of wetting: from inertial spreading to viscous imbibition. *J. Phys.: Condens. Matter* **2009**, 21, 464127, DOI: 10.1088/0953-8984/21/46/464127.

(42) Chen, L.; Bonaccurso, E. Effects of surface wettability and liquid viscosity on the dynamic wetting of individual drops. *Phys. Rev. E* **2014**, 90, 022401, DOI: 10.1103/PhysRevE.90.022401.

(43) Saiz, E.; Tomsia, A. P.; Rauch, N.; Scheu, C.; Ruehle, M.; Benhassine, M.; Seveno, D.; de ConinckEsteb, J. Nonreactive spreading at high temperature: molten metals and oxides on molybdenum. *Phys. Rev. E* **2007**, 76, 041602, DOI: 10.1103/PhysRevE.76.041602.

(44) Bird, J. C.; Mandre, S.; Stone, H. A. Short-Time dynamics of partial wetting. *Phys. Rev. Let.*, **2008**, 100, 234501, DOI: 10.1103/PhysRevLett.100.234501.

Supporting Information File

Wetting and spreading of molten volcanic ash in jet engines

*Wenjia Song** [†], *Yan Lavallée* [‡], *Fabian B. Wadsworth*[†], *Kai-Uwe Hess*[†], *and Donald B. Dingwell*[†]

[†] Department of Earth and Environmental Sciences, Ludwig-Maximilians-Universität München, Theresienstrasse 41, 80333 Munich, Germany.

[‡] Earth, Ocean and Ecological Sciences, University of Liverpool, Liverpool, L69 3GP, U.K.

***Corresponding author**: Wenjia Song (wenjia.song@lmu.de)

Contents of this file

Additional Supporting Information

Introduction

The supporting information here provides additional technical details on the Eyjafjallajökull volcanic ash characterization, measurement of the sample temperature, definition of characteristic conditions in spreading process, definition of average spreading velocity, viscosity measurement of volcanic ash melt, the sensitization of molten volcanic ash on interfacial effects, rescaling the spreading process based on Tanner'law, Pearson product-moment correlation coefficient analysis as well as movie for showing the wettability and spreading process of volcanic ash at the extreme heating conditions

Text S1.

Eyjafjallajökull volcanic ash characterization: X-ray fluorescence (Philips Magix XRF spectrometer at 4 kV) and scanning electron microscope (SEM, JEOL JSM-5600) analyses were conducted on samples to assess their bulk chemical composition (Figure S1A) and to observe the microstructure of the ash particles (Figure S1B). Particle size distributions of milled ash were measured via a LS 230 laser diffraction particle analyser (Beckman Coulter) (Figure S1C). The D_{10}, D_{50} and D_{90} values in Figure S1C constrain the smallest particle size, which contribute to define the coarsest 10%, 50% and 90% particle fraction from the cumulative volume distribution, respectively.

Text S2.

Measurement of the sample temperature: In the current optical dilatometer apparatus, the thermocouple and insulation are inserted into an alumina protection tube (Figure S2A), which is generally used to measure the sample temperature at controlled heating rates (e.g., $\leq 10°C\ min^{-1}$). However, due to the effect of a lag in heat transfer through the alumina protection tube, we

adopted a new temperature measurement procedure by drilling two small holes (1 mm diameter) in the protection tube wall and the alumina substrate, and placing the joint/tip of the thermocouple onto the alumina substrate in the same position as the volcanic ash compact core (Figure S2B). This yields a measured temperature closer to that of the ash compact. Subsequently, we carried out the same insertion procedure as utilized in the series of wetting experiments described in the main text; namely, rapidly mitigating the thermocouple with joint being outside of the protection tube to the hot zone of the furnace heated to the highest temperature $\boldsymbol{T_{max}}$ between 1039°C and 1451°C with temperature intervals of 47°C, and maintaining 600s until thermodynamic equilibrium and then extrapolating the same exposure time as the volcanic ash wetting experiment. The heating profile experienced by the thermocouple with the joint that is outside the protective tube is recorded (black line in Figure S2C) and consequently, is compared to those with the joint inside of the protective tube obtained in the wetting experiments (red line in Figure S2C).

Subsequently, to quantify the rate of heat transfer in the heating process with two different rates, we calculated the average heating rate using Eq. (1).

$$\bar{q} = \frac{\sum_{i=1}^{n=t_t} \frac{dT_i}{dt_i}}{n} \; i = 1,\ldots,n \tag{1}$$

Where, $\overline{\boldsymbol{q}}$ is the average heating rate (°C s^{-1}), $\boldsymbol{T_i}$ is the measured temperature at time $\boldsymbol{t_i}$, and $\boldsymbol{t_t}$ is defined as the time when the temperature equals to the 99% of the equilibrium temperature and also regarded as the threshold value between the non-isothermal and isothermal region. The use of this parameter $\boldsymbol{t_t}$ reduces the influence of the cross-section of the heating profile. From analysis of average heating rate shown in Figure S3, we note that $\overline{\boldsymbol{q}}$ measured by the joint of the

thermocouple directly exposed to the hot zone at the various $\boldsymbol{T_{max}}$ are always higher than those where the joint of thermocouple is within the protection tube. Hence, we regard the measured temperature profiles by the thermocouple whose joint is the outside of the protection tube as that realistically experienced by ash compact in the wetting experiment.

Text S3.

Definition of the area percentage: During the melting process, the absolute value of the specimen silhouette area is calculated by the number of pixels in the samples. Subsequently, the area percentage, A%, is defined by Eq. (3):

$$A(\%) = \frac{(P_{in} - P_{(t,T)})}{P_{20}} \tag{3}$$

where P_{in} and P are the number of the pixel included a sample core's silhouette at the initial stage and the area after each interval time (t) or temperature (T), respectively. The relationship between the area percentage and time at different temperatures is shown in Figure S4.

Text S4.

Definition of characteristic conditions in spreading process: In the present study, through an analysis of the geometrical evolution of the volcanic ash compact, we note that spreading of molten volcanic ash droplets is distinct from the traditional liquid spreading process; Owing to the overlap of the processes of melting and spreading of the molten volcanic ash droplet, it is thus necessary to re-define the various characteristic conditions which dictate the spreading process of the molten volcanic ash droplet. Based on the evolution of radius r between the molten volcanic ash and solid alumina substrate in the whole experimental process, we define the initial, final and equilibrium spreading conditions, respectively, as follows. The initial spreading

condition is defined when the radius $\boldsymbol{r}$ becomes small and then constantly increases with time and the corresponding radius and time are regarded as the initial spreading radius $\boldsymbol{r_I}$ and the initial spreading time $\boldsymbol{t_I}$ (red circle symbols in Figure S5). Defining an explicit point as the finial spreading condition is not straightforward because wetting is a subject in which disorder plays an important role, even under idealized laboratory conditions (e.g., an ideal liquid wetted on a non-chemical reaction substrate, such as a water droplet spread on a glass surface at room temperature). In order to diminish the effect of disorder shown in the crossover of radius curves at each $\boldsymbol{T_{max}}$, we regard the condition when *r* is equal to 90% of the equilibrium condition (namely, where the experiment finishes, see color square symbols in Figure S5) as the final spreading condition (black square symbols in Figure S5). Consequently, the final and equilibrium conditions corresponding to the radii and time are considered as final spreading radius $\boldsymbol{r_F}$ and equilibrium radius $\boldsymbol{r_{eq}}$ as well as final spreading time $\boldsymbol{t_F}$ and equilibrium time $\boldsymbol{t_{eq}}$. Furthermore, according to the evolution of shape factor *S,* which is defined by droplet circularity, a function of the perimeter $\boldsymbol{P}$ and the area $\boldsymbol{A}$ of the silhouette of volcanic ash droplet (see Eq. (2))

$$S = \frac{4\pi A}{P^2} \tag{2}$$

where the *S* of a circle is 1. After passing the initial spreading condition, the droplet radius $\boldsymbol{R}$ is measured when the shape factor value *S* becomes the maximum (pink diamond symbols in Figure S5). All characteristic conditions corresponding to times and radii at three independent times are shown in Table 1.

Text S5.

Definition of average spreading velocity: In order to quantify the spreading dynamics, we estimate the average spreading velocity $\overline{\boldsymbol{v}}$ by calculating the average value of the instantaneous velocity at each second during the spreading process occurring between the initial and finial spreading conditions (Eq. (4)).

$$\bar{v} = \frac{\sum_{t=1}^{t=\Delta t} \left(\frac{d\,\mathrm{r}_r}{dt_r} \right)_i}{\Delta t} \; i = 1, \ldots, \Delta t \tag{4}$$

where $\Delta t = t_F - t_I$, $\boldsymbol{t_I}$ and $\boldsymbol{t_F}$ are the initial and final spreading time, respectively. $\boldsymbol{r_r}$ is the relative spreading radius (equal to the difference between the absolute spreading radius and the initial spreading radius, $\boldsymbol{r - r_r}$), $\boldsymbol{t_r}$ is the relative spreading time (equal to the difference between the absolute spreading time and the initial spreading time, $\boldsymbol{t - t_r}$).

Text S6.

Viscosity measurement of volcanic ash melt: High temperature viscosity measurements of volcanic ash melt were obtained using the concentric cylinder system. The starting materials for viscosity determinations were melt glasses prepared from Eyjafjallajökull volcanic ash. Approximately 50 g of ash materials were first ground in alcohol in an agate mortar for 3 hours and then heated at 800 °C overnight to remove any organic carbon products. These samples were fused at 1400 °C for 3 hours in a 25 cm^3 Pt crucible. Prior to viscosity determinations, fused samples were poured from the Pt crucible into the $Pt_{80}Rh_{20}$ crucible used for viscosity measurement.

Viscosity was measured with a Brookfield RVTD viscometer head at 1 atm in the temperature range from 1395 °C to 1199 °C by cooling in 20 °C increments. Measurement was started at 1500 °C (corresponding to sample temperature of 1395 °C) and the melt was stirred with a $Pt_{80}Rh_{20}$ spindle for 1 hour, resulting in a homogenous, bubble-free melt. Subsequent measurements were performed in increments of decreasing temperature until crystallization occurred (Figure S6A).

Note that, in the current wetting experiment, the whole spreading process of molten volcanic ash is partially combined with the fusion process, which causes complications as the droplet is not a homogenous liquid, but rather includes crystals and bubbles. This may imply that the rheological properties are not Newtonian. We use the model based on the experimental viscosity values estimated in Figure S6B obtained from the volcanic ash melt without crystals and bubble in the thermodynamic equilibrium condition. However, considering the influence of bubble and crystals in the partial and complete spreading process at each T_{max} conditions on viscosity, it might result in the certain error.

Text S7.

The sensitivity of molten volcanic ash on interfacial effects: In the high temperature system, the interfacial reaction between sample and substrate is inevitable. It might be that the degree to which the interfacial reaction and dissolution between molten volcanic ash and alumina substrate is a function of temperature. Thus, we first analyzed the most extreme case, namely, the sample which remained at the highest temperature of 1451°C for 5000 s to determine the effect of interfacial effects on spreading process in our current experiment.

We performed cross-section analyses of the drop and substrate interface after the experiment using an electron probe micro-analyzer to quantitatively measure the chemical composition of

the volcanic ash sample after experiment (Figure S7A). Because viscosity – a chemically-defined parameters of silicate liquids – is the most influential factor in the determination of the spreading kinetics of molten volcanic ash, the relative modification of viscosity due to the dissolution of alumina was estimated (see below) at < 2%, which indicates interfacial effects in our experiment can be regarded as negligible; that is, all of spreading process in our current experimental conditions can be regarded as nonreactive spreading process. Here, due to the fact that it is impossible to directly measure the viscosity of heterogeneous volcanic ash sample during the physico-chemical process of fusion and wetting studied here, the viscosity at each furnace temperature is estimated using the bulk chemical composition of the ash as input parameter into the GRD silicate melt viscosity calculator (Figure S7B).

Text S8.

Rescaling the spreading process based on Tanner's law: Tanner's law assumes that viscous forces are the dominant source of resistance and uses a capillary time scale to derive a power-law time dependence between the spreading radius, $\boldsymbol{r}$ and time $\boldsymbol{t}$ of $\boldsymbol{r} \sim \boldsymbol{t^a}$. Here, we characterized the spreading behavior by dimensional analysis $\boldsymbol{r_r/R = C(t_r/\tau)^a}$, where $\boldsymbol{r_r}$ and $\boldsymbol{t_r}$ are the relative spreading radius and relative spreading time, with a prefactor $\boldsymbol{C}$ and a power-law exponent $\boldsymbol{a}$, the capillary time is given by $\boldsymbol{\tau = R\mu/\Gamma}$ with $\boldsymbol{\mu(T,t)}$, $\boldsymbol{R}$ and Γ the dynamic viscosity, droplet radius and surface tension. Except for the spreading processes at 1133 °C and 1180 °C, which is isothermal, all the experiments experience non-isothermal conditions. Accordingly, the viscosity of molten volcanic ash droplet is no longer constant but varies with time and temperature in the spreading process. This is one of the biggest differences between the low and high temperature spreading of organic liquids and polymers, and molten metals. Thus, dynamic viscosity $\boldsymbol{\mu(T,t)}$ is

calculated via the specific regression expression shown in Figure 4 based on each spreading time for a given temperature condition.

Text S9.

Pearson product-moment correlation coefficient analysis: Figure S8 shows the logarithm of the normalized relative radius, $\log(r_r/R)$, as a function of the logarithm of the normalized relative time, $\log(t_r/\tau)$ for the whole spreading process of the molten volcanic ash at the T_{max} range of 1133-1451°C. The spreading kinetics shown in Figure S8 do not follow an ideal power law relationship between t_I until t_F at the various T_{max}.

First, we used the Pearson product-moment correlation coefficient ζ (Eq. (5)) to analyze the power law relationship between r_r/R and t_r/τ between t_I and t_F at the T_{max} range of 1133-1451 °C.

$$\xi = \frac{\sum_{i=1}^{n}(\log(r/R)_i' - \frac{1}{n}\sum_{i=1}^{n}\overline{\log(r/R)_i}')(\log(t/\tau)_i' - \frac{1}{n}\sum_{i=1}^{n}\overline{(t/\tau)_i}')}{\sqrt{\sum_{i=1}^{n}(\log(r/R)_i' - \frac{1}{n}\sum_{i=1}^{n}\overline{\log(r/R)_i}')^2}\sqrt{\sum_{i=1}^{n}(\log(t/\tau)_i' - \frac{1}{n}\sum_{i=1}^{n}\overline{(t/\tau)_i}')^2}} \; i = 1,\ldots,n \tag{5}$$

ζ has a value between -1 and 1. ζ of -1 or 1 corresponds to a very good linear relationship between $\log(r_r/R)$ and $\log(t_r/\tau)$, indicting there is a power law relationship between r_r/R and t_r/τ and the spreading process perfectly follows Tanner's law.

According to the variation of ζ marked in blue circles throughout the whole spreading process, we define the time of lowest ζ as time t_c and take this as the threshold point between the early and later stages. After this point, we reapplied the Pearson product-moment correlation coefficient ζ to analyze the power law relationship between log (r_r/R) and log (t_r/τ) in the stage between the t_c and t_F, and the ζ value in between t_c and t_F, and determined it to be higher

than 0.99 (that is, there is a power law relationship between them). At $\boldsymbol{T_{max}}$ of 1133 °C, where we found that ζ is low (< 0.4), due to the fact that spreading is not continuous in this experiment.

A

Chemical composition (wt.%)								
SiO_2	Al_2O_3	FeO	CaO	K_2O	Na_2O	MgO	TiO_2	MnO
59.68	15.70	7.99	4.53	2.28	5.59	2.39	1.37	0.21

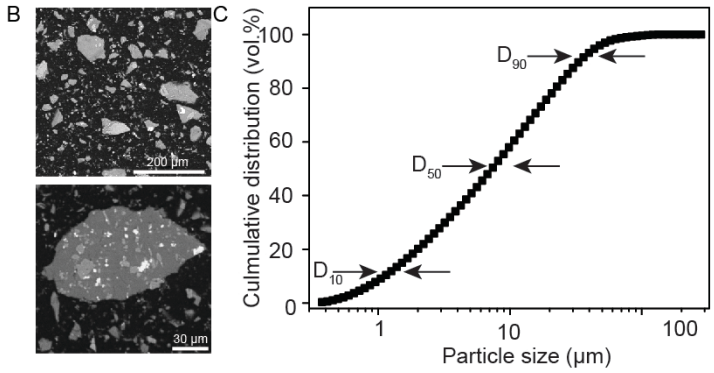

Figure S1. Physical and chemical characteristics of the Eyjafjallajökull volcanic ash. (A) The bulk chemical composition constrained by the major oxides content (wt.%). (B) SEM images of embedded volcanic ash particles (left) and a single ash particle (right). (C) Cumulative volume distribution of the milled ash.

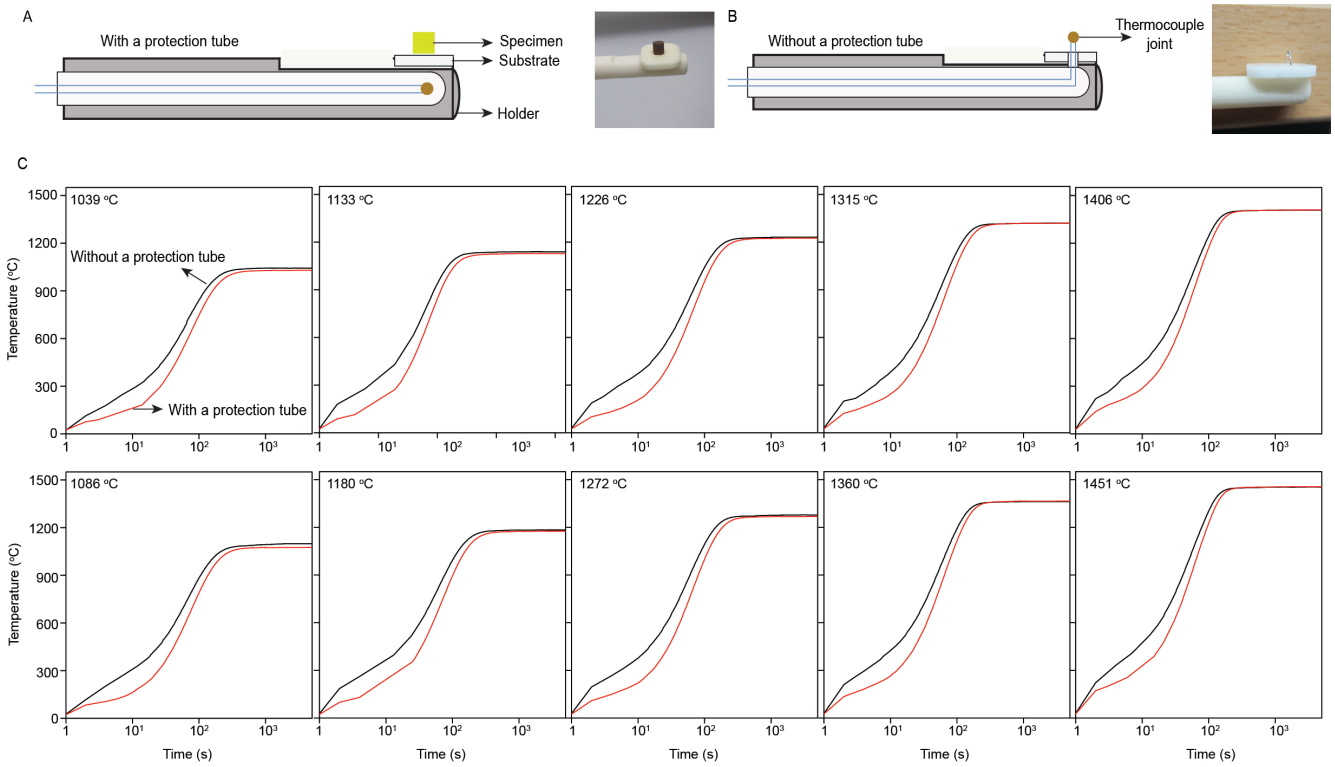

Figure S2. Measurement of sample temperature. (A) Side view sketch and image of an ash sample and alumina substrate on the specimen holder; note the position of the thermocouple in a protective tube. (B) Side view sketch and image of the joint of an unprotected thermocouple in an alumina substrate specimen holder. (C) The heating profile obtained from the thermocouple with (red lines) and without (black lines) protection tube as a function of time at the $\boldsymbol{T_{max}}$ range from 1039 °C to 1451 °C. The temperature value of the thermocouple with protection tube is the mean of 3 independent experiments.

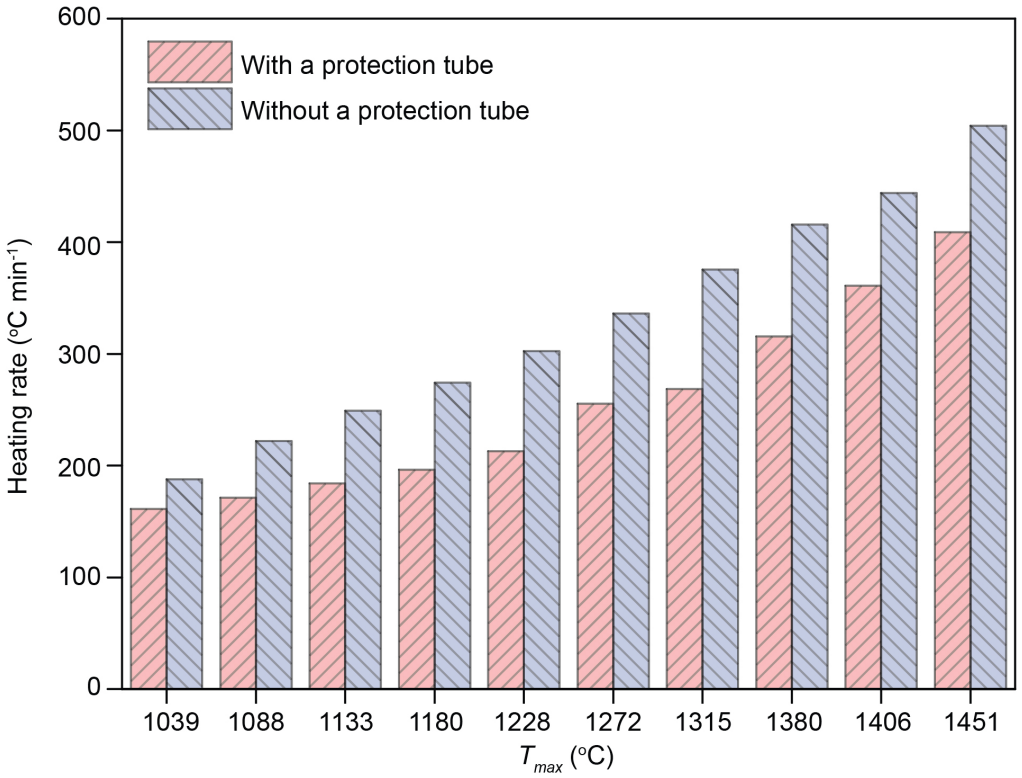

Figure S3. Comparison of heating rates obtained by the thermocouple with and without protection tube at the $\boldsymbol{T_{max}}$ range from 1039 °C to 1451 °C.

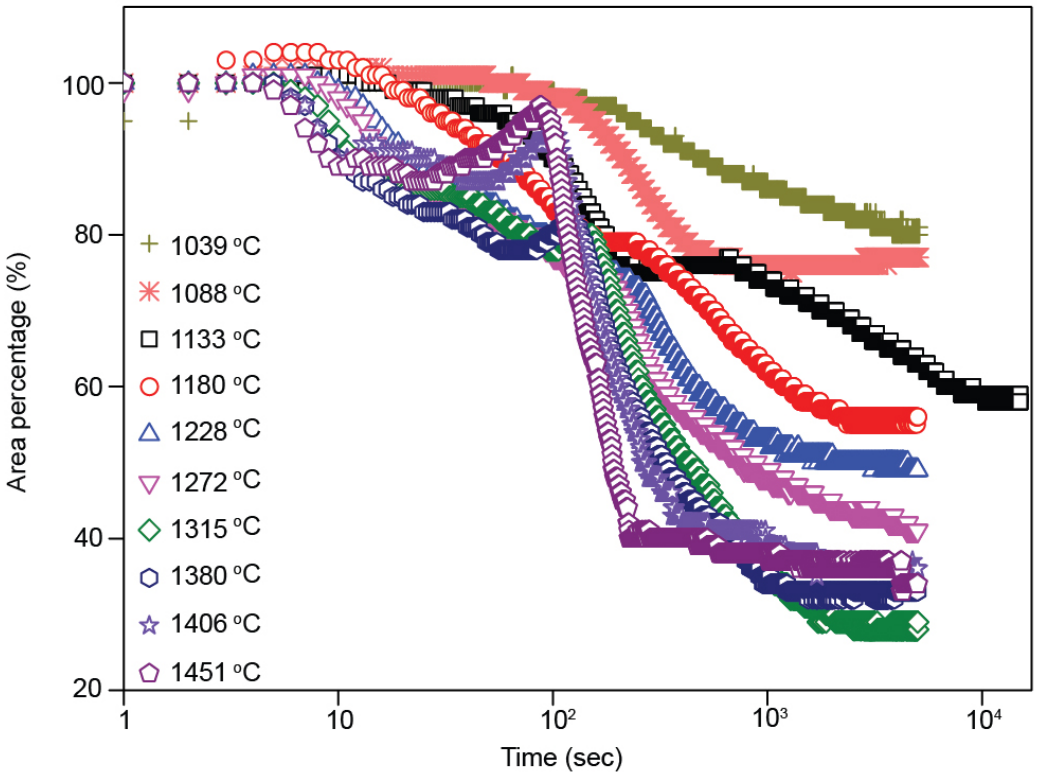

Figure S4. The evaluation of area percentage of a cylindrically shaped volcanic ash compact sample at the $\boldsymbol{T_{max}}$ range from 1039 °C to 1451 °C.

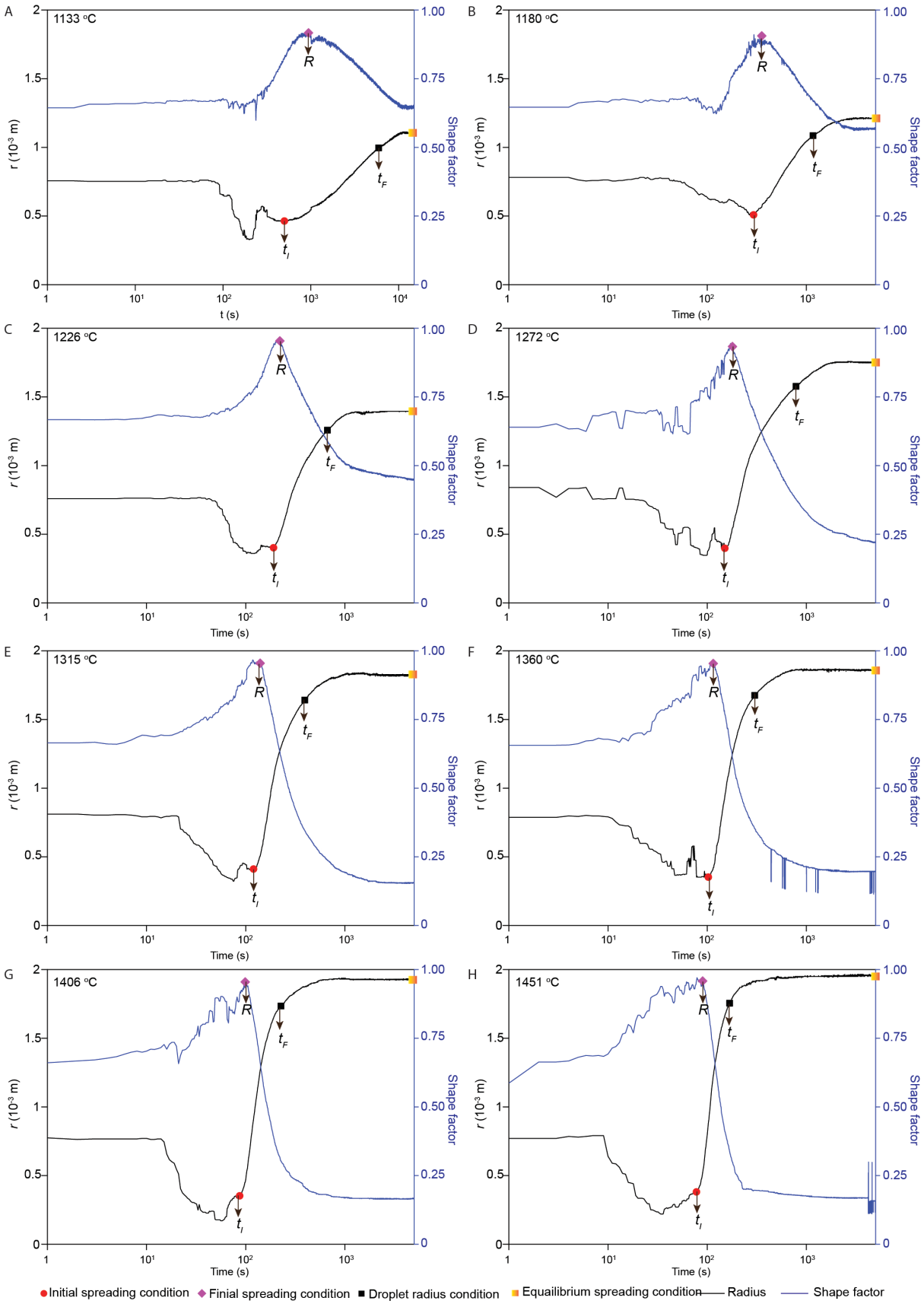
A
1133 °C
B
1180 °C
C
1226 °C
D
1272 °C
E
1315 °C
F
1360 °C
G
1406 °C
H
1451 °C
r (10⁻³ m)
Shape factor
t (s)
Time (s)
R
t_F
t_I
Initial spreading condition
Finial spreading condition
Droplet radius condition
Equailibrium spreading condition
Radius
Shape factor

Figure S5. Definition of various characteristic conditions in the spreading process experienced by molten volcanic ash droplet at the $\boldsymbol{T_{max}}$ range from 1133 °C to 1451 °C. Evolution of the spreading radius *r* and shape factor *f* of the molten volcanic ash droplet is displayed as a function of time at the various $\boldsymbol{T_{max}}$. The results are the representative of 1 independent experiment.

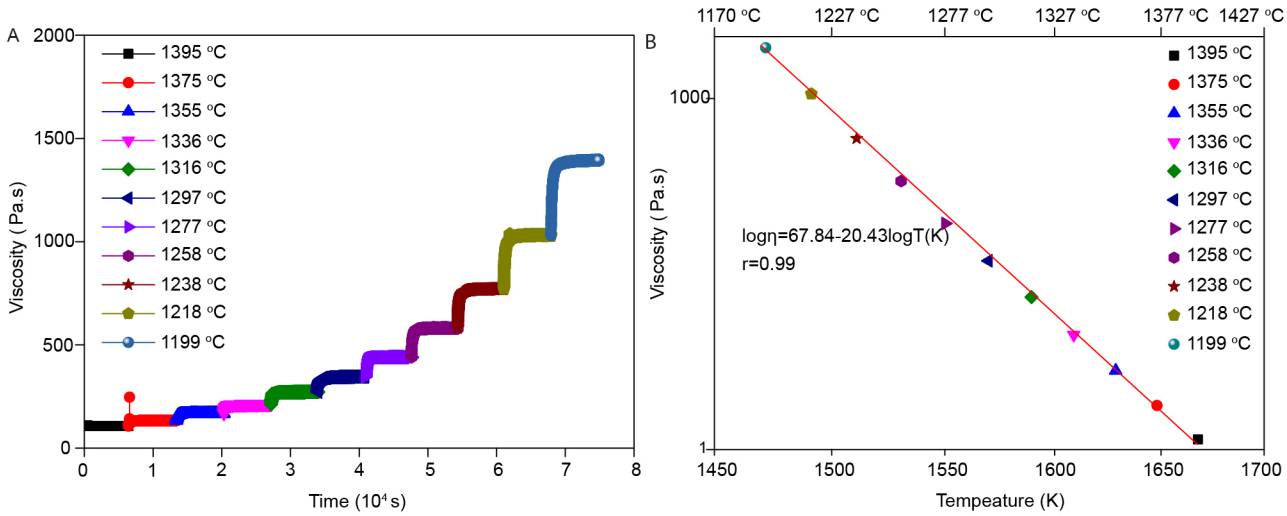

Figure S6. Viscosity-temperature relationships for the volcanic ash melt. (A) The viscosity of volcanic ash melt as a function of time at the temperature range from 1199 °C to 1395 °C. (B) The viscosity data obtained for the volcanic ash melt at the equilibrium condition are fitted with a regression for which the equation is given in the figure along with the goodness of fit.

A

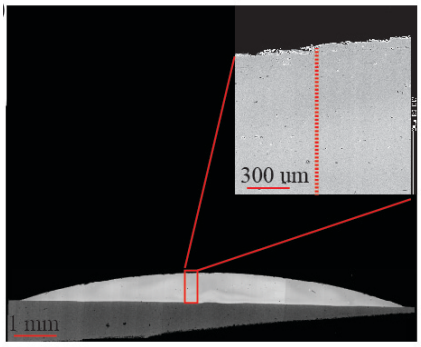

B

Chemical Composition (wt%)	Before Experiment	After Experiment
SiO_2	59.68	58.59
Al_2O_3	15.70	21.01
FeO	7.99	6.63
CaO	4.53	4.34
K_2O	2.28	2.16
Na_2O	5.59	3.81
MgO	2.39	1.92
TiO_2	1.37	1.33
MnO	0.21	0.22
Viscosity (Pa.s)	54.95	51.28

Figure S7. The effect of interfacial reactions. (A) Cross-sectional scanning electron micrograph of the interface between molten volcanic ash droplet and an alumina substrate on the chemical composition of molten volcanic ash droplet after spreading at the $\boldsymbol{T_{max}}$ of 1451 °C. The inset is a partial enlarged section of Figure S7A where the chemical composition of red dashed line was measured by electron probe micro analysis. (B) Comparison of the bulk chemical composition (in wt. % of oxides) of the volcanic ash measured by X-ray fluorescence before experiment and average value of the chemical compositions of 270 points distributed in the line shown in Figure S7A after experiment as well as the corresponding viscosity calculated by GRD model based on these two chemical compositions and a temperature of 1451 °C.

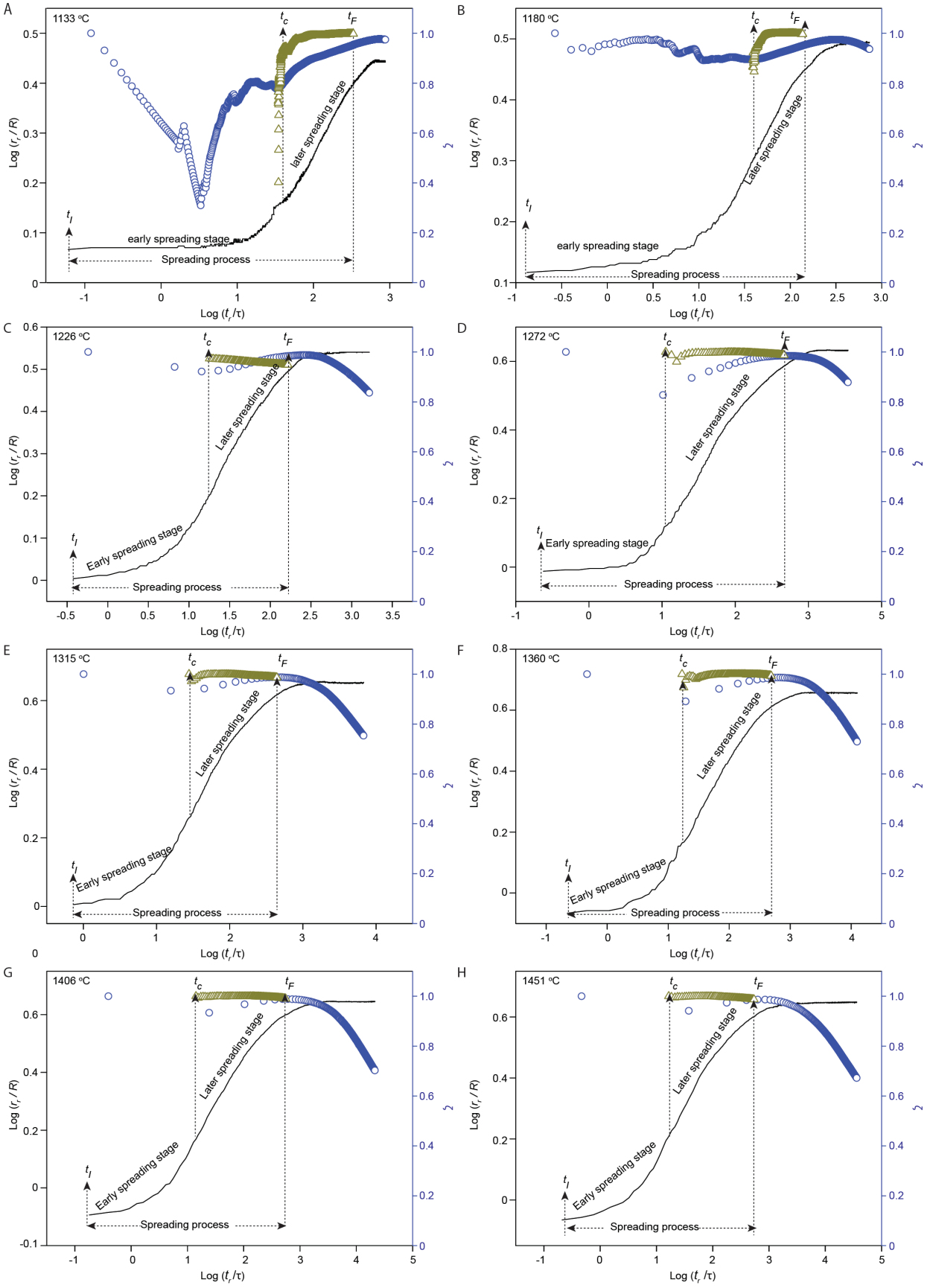
A
1133 °C
B
1180 °C
C
1226 °C
D
1272 °C
E
1315 °C
F
1360 °C
G
1406 °C
H
1451 °C
t_c
t_F
t_I
later spreading stage
Later spreading stage
Early spreading stage
early spreading stage
Spreading process
Log (r_r / R)
Log (t_r /τ)
ζ

Figure S8. Rescaling experimental data on the spreading process for the molten volcanic ash droplet at the $\boldsymbol{T_{max}}$ range from 1133 °C to 1451 °C. The logarithm normalized spreading relative radius, log (r_r/R) (black line), and the corresponding linear correlation coefficient ζ in the whole spreading process (blue circles) and between the t_c and t_F (yellow triangles) as a function of the logarithm of normalized time, log (t_r/τ). The results are the representative of 1 independent experiment. A reduced dataset is shown for clarity.

Table S1. The parameters at the characteristic conditions in the spreading process experienced by molten volcanic ash droplet at the T_{max} range from 1133 °C to 1451 °C. The data is provided for three runs and the average is calculated along with the standard deviation.

Temperature (°C)	Time	Equilibrium conditions						Dynamic process			
		$\theta_{eq,L}$ (°)	$\theta_{eq,R}$ (°)	$\theta_{eq,}$ (°)	r_{eq} (10^{-3} m)	t_I (s)	t_F (s)	$\bar{v}$ (10^{-5} m s^{-1})	a	C	r
1133	1st	69	69	69	2.20	500	5918	0.020	0.27	0.52	0.99
	2nd	70	71	71	2.20	552	6250	0.022	0.32	0.30	0.99
	3rd	74	72	73	2.24	549	5388	0.023	0.30	0.29	0.99
	Mean ± s.d.	71±2.08	71±0.69	71±2.02	2.21±0.022	534±29.19	5852±434.77	0.022±0.001	0.30±0.025	0.37±0.13	0.99
1180	1st	63	64	64	2.42	268	1235	0.12	0.27	0.75	0.99
	2nd	63	64	64	2.43	294	1170	0.13	0.24	0.73	0.99
	3rd	67	66	67	2.39	294	1197	0.14	0.25	0.87	0.99
	Mean ± s.d.	65±2.31	65±1.15	65±1.73	2.41±0.018	285±15.01	1201±32.65	0.13±0.001	0.25±0.015	0.78±0.076	0.99
1226	1st	50	50	50	2.69	195	608	0.37	0.29	0.65	0.99
	2nd	51	50	51	2.79	191	667	0.36	0.29	0.74	0.99
	3rd	52	50	51	2.82	201	705	0.34	0.25	0.87	0.99
	Mean ± s.d.	51±0.58	50±0	51±0.50	2.76±0.069	196±5.03	660±48.88	0.36±0.001	0.28±0.023	0.75±0.11	0.99
1272	1st	29	28	29	3.48	151	771	0.38	0.28	0.70	0.99
	2nd	25	25	25	3.48	157	801	0.36	0.25	0.84	0.99
	3rd	27	27	27	3.51	151	790	0.37	0.30	0.58	0.99
	Mean ± s.d.	27±2.00	27±1.53	27±1.76	3.49±0.02	153±3.64	787±15.18	0.37±0.001	0.28±0.025	0.71±0.13	0.99
1315	1st	22	22	22	3.66	120	395	0.89	0.28	0.92	0.97
	2nd	21	21	21	3.63	128	448	0.77	0.25	0.86	0.99
	3rd	23	23	23	3.60	128	446	0.76	0.26	0.84	0.99
	Mean ± s.d.	22±1.00	22±1.00	22±1.00	3.63±0.028	125±4.62	430±30.04	0.08±0.001	0.26±0.015	0.87±0.04	0.99
1360	1st	21	20	21	3.72	103	302	1.32	0.31	0.60	0.99
	2nd	20	21	21	3.72	92	253	1.64	0.36	0.50	0.99
	3rd	20	20	20	3.72	105	285	1.43	0.26	0.84	0.99
	Mean ± s.d.	21±0.29	21±0.29	21±0.29	3.72±0	100±7.00	280±24.88	1.47±0.001	0.31±0.05	0.65±0.17	0.99
1406	1st	19	19	19	3.87	78	199	2.23	0.26	0.52	0.99
	2nd	19	19	19	3.86	87	227	1.98	0.29	0.30	0.99
	3rd	19	20	20	3.88	93	228	2.02	0.25	0.29	0.99
	Mean ± s.d.	19±0	19±0.57	19±0.57	3.87±0.008	86±7.55	218±16.46	2.10±0.001	0.27±0.02	0.37±0.13	0.99
1451	1st	18	18	18	7.84	78	169	3.03	0.25	0.80	0.98
	2nd	18	19	19	7.83	66	153	3.13	0.26	0.81	0.99
	3rd	18	19	19	7.84	74	182	2.60	0.26	0.77	0.99
	Mean ± s.d.	18±0	18±0.57	18±0.57	7.84±0.01	73±6.11	168±14.52	2.92±0.28	0.26±0.0058	0.79±0.02	0.99

Movie S1. the wettability and spreading process of volcanic ash at the extreme heating conditions.